Title
IMAGING PERFORMANCE EVALUATION OF AN ADVANCED PET SYSTEM

Permalink
https://escholarship.org/uc/item/4691q0s2

Author
Xing, Yan

Publication Date
2012

Peer reviewed|Thesis/dissertation

IMAGING PERFORMANCE EVALUATION OF AN
ADVANCED PET SYSTEM

by

YAN XING

THESIS

Submitted in partial satisfaction of the requirements for the degree of

MASTER OF SCIENCE

in

Biomedical Imaging

in the

GRADUATE DIVISION

of the

UNIVERSITY OF CALIFORNIA, SAN FRANCISCO

DEDICATION AND ACKNOWLEDGEMENTS

IMAGING PERFORMANCE EVALUATION OF AN ADVANCED PET SYSTEM

ABSTRACT

In the development of new PET/CT systems, image quality assessment is critical. This study evaluated two aspects of system performance on a PET/CT scanner under development: the displacement of the source of radioactivity off the center of the field of view and the reconstruction algorithm employed for the correction of metal artifacts. Uniformity served as the principal property for image quality assessment in both studies. Our findings indicated that the displacement from the center resulted in increased non-uniformity, particularly at the edge, and the activity concentration and standard uptake value inaccuracies worsened with increased degree of displacement. Further, the in-built whole-body metal contrast reconstruction failed to correct for the metal artifact for metal plates with a thickness up to 3cm. These results shed light to the potential improvements of system image quality and provide grounds for future work on performance testing with better clinical representations.

TABLE OF CONTEXT

LIST OF FIGURES

I. INTRODUCTION

The major goal in the development of positron emission tomography (PET) with attenuation corrected by computer tomography (CT), i.e. the PET/CT scanners is to obtain good image quality with accurate location and intensity of signal sources (1). Image quality is a semi-quantitative metric, which can be assessed by both qualitative and quantitative means (2). The NU 2-2007 published by the National Electrical Manufacturers' Association (NEMA) (3) is widely recognized for quantitatively characterizing the performance of PET scanners. The document specifies procedures for acquiring and analyzing data using standard phantoms and sources (4). It incorporates a spectrum of critical parameters associated with good image quality formation, including spatial resolution, sensitivity, noise, scattered radiation, and contrast. The imaging industry generally requires performance tests on newly developed PET/CT scanners for quality assurance. The performance tests, however, are not limited to NEMA assessments: any situations with clinical relevance where the image quality could potentially be distorted should be assessed by phantoms and sources at the research and development stage.

In this report, a PET/CT system under development at Philips Healthcare, which is similar to the established Philips Gemini TF PET/CT system (5), was selected for study. Two situations that may impact the image quality in clinical settings, which are not yet studied in the system development, are assessed by the germanium-68 cylindrical phantoms. The first study pertains to the displacement off the center of the radioactive source. In this study, the

radioactive source is displaced away from the center of the field of view (FOV) in four principal directions to both intermediate and extreme degrees. This investigation is particularly relevant to whole-body scanning for large patients, where radioactive source uptake may be located off the center of the FOV. The potential non-uniformity issue when the radioactive source is located off the center of FOV has been reported in previous literature (6). With the newly implemented PET detector technology and the improved reconstruction algorithm under development in this system, we hypothesize that the image quality should remain unchanged (or minimally compromised) when the radioactive source is located off center for the scanner of study. The second study relates to the in-built whole-body metal contrast reconstruction of the scanner for patients with metallic implants. These metallic implants, such as hip prosthetics and chemotherapy ports, result in high CT numbers and metal streaking artifacts because of their high proton absorption (7,8). The correspondingly elevated PET activity concentration from the high Hounsfield units, could lead to an overestimation of PET activity and thereby to false-positive PET findings (9). We hypothesize that the in-built reconstruction algorithm effectively corrects for the elevated PET activity with the presence of both small and large amounts of metal – the function that the conventional whole-body attenuation-corrected reconstruction fails to provide.

Image uniformity serves as the principal property for image quality assessment in the study. Uniformity measures the deviation of a reconstructed image from the uniform response that is the ideal outcome for a

homogenous radioactive source (10). Uniformity reflects the system sensitivity and specificity (11) and its ability for accurate quantification of PET signal (12). The challenge in uniformity assessment is that there may be large regional heterogeneity, which will be diluted in a global analysis. It is therefore preferable to employ both regional and global assessments (13). Moreover, no stringent acceptance criteria exist to assess for uniformity; therefore multiple metrics including standard deviation and line profiles are used to reach a more valid conclusion.

II. METHODS

1. OFF-CENTER STUDY

A. Data acquisitions

A germanium-68 cylindrical phantom was used as the radioactive source for the PET/CT study due to the reasonable half-life (271 days) of the Ge-68 source in addition to the ease of generation, storage and usage (14). The activity concentration of parent Ge-68 on the date of measurement was recorded. All data acquisitions were performed using a whole-body PET/CT scan and the standard whole-body reconstruction, where the surview image that is served as an overview for the CT image selection, a CT image, non-attenuated-corrected PET image (NAC-PET) and attenuation-corrected PET image (CTAC-PET) were acquired. The frontal CT surview was used with the default parameters and at least one bed at the center of the phantom was needed. PET images with counts between 50 million and 100 million were acquired. Only the central bed was needed in the PET acquisition and reconstruction process.

Displacements in the horizontal and vertical directions were assessed. The center of the Ge-68 phantom was marked prior to scanning. The reference scan at the center was acquired by co-localizing the phantom center with the center of the CT scanner, as indicated by the two-dimensional laser beams.

Vertical Direction: When the pellet was displaced in the vertical direction, two sets of images were acquired when the pellet bed was moved to the uppermost position and lowermost position respectively in the allowable pellet position range. The displaced distances were recorded from the scanner display. An uppermost position was also reached where the phantom touched the cover of the PET scanner. This was achieved by placing sponges and plastic wraps underneath the phantom where the pellet was placed at the uppermost position. No metal holder was introduced to avoid artifacts. *Figure 1* demonstrates how the uppermost position was achieved.

Figure 1: The uppermost position of the phantom.

Horizontal Direction: The diameters of the CT and PET bores and of the Ge-68 phantom were measured by a measuring ruler. The radius (*r*) of the CT and of the PET should be very similar and was calculated as the average of the two.

The Ge-68 phantom (with a radius of *p*) was moved a distance of (*r-2p*) towards the left- and right-side of the scanner to reach the far edge of the lateral direction. The phantom was subsequently placed at two intermediate lateral positions displaced (*r-2p*) /2 to the left and right of the scanner center. The laterally displaced phantom was held in place by package sponge and paper towels. No metal holder was used to avoid metal artifacts in the CT scan. Data acquisitions were performed at these four lateral positions (as illustrated in *Figure 2*). Since the pallet is curved, it is important to adjust the vertical level of the phantom (as indicated in the CT image) to ensure that everything stayed at the same horizontal level when laterally displaced.

(a)   (b)
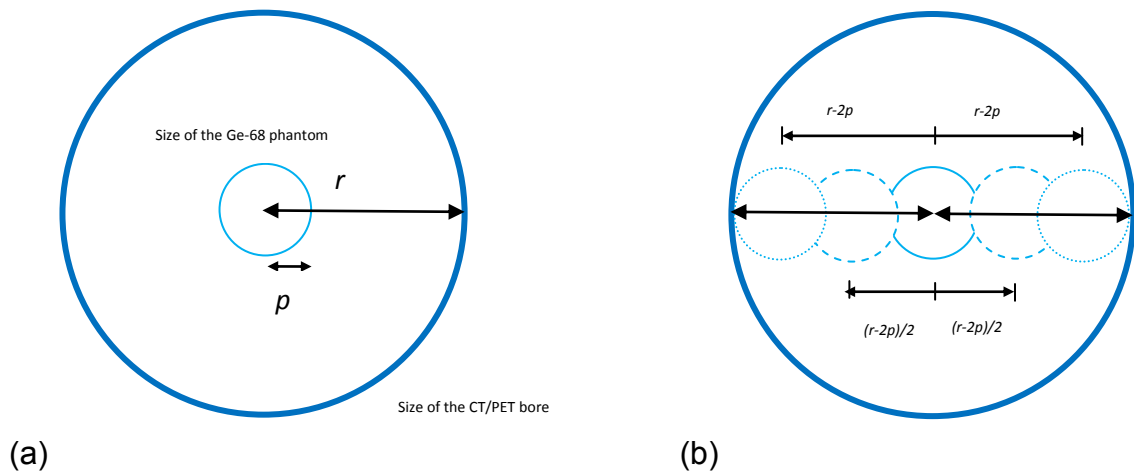
Figure 2: (a) The position of the phantom in the reference scan (at the center of the bore). **(b)** The positions of two laterally displaced phantoms in reference to the center and the edge of the scanner (as indicated by the dash line).

B. Image Quality Analysis

(a). Qualitative Analysis

The CT images and the CTAC-PET reconstructed images were interpreted visually for any possible artifacts. The artifacts could cause the distortion of the uniformity and homogeneity of the phantom, significant elevation in the noise level and reduced spatial resolution. All the artifacts were recorded and described at every displaced position.

(b). Quantitative Analysis

All the quantitative performance tests adhered to the NEMA NU 2-2007 standard (3). The scan where the phantom was placed at the center of the scanner was regarded as the standard of reference.

ImageJ image processing tool was employed as the primary image processing tool (National Institute of Health, U.S.A) and *Matlab* (Matlab R2009a, The Mathworks Inc., Natick, MA, U.S.A) scripts were used to supplement analysis. Image quality was assessed by drawing regions of interest (ROI) centered at the center of the circular phantom with an area covering at least 80% of the total radioactive area. The ROI was ideally maintained constantly positioned with a similar area in all the phantom analyses. The ROI area, the mean activity concentration, the minimum and maximum activity concentration, the standard deviation and slice number were recorded. The activity concentrations were plotted against the slice number for all phantom positions. The center position was used as the standard of reference. The percentage difference of the activity concentration at the other positions was calculated accordingly. Standard uptake values (SUVs) were also calculated for each slice with equation [1] and were

6

plotted against the slice number. This was achieved by 'readcentroid.m' matlab script developed by the system analysis group (The scripts are shown in Appendix B).

$$SUV(t) = \frac{c(t)}{injected\ activity\ /\ body\ weight}$$ [1]

The ROI measurement in the central slice was selected, as well as 5 slices above and 5 slices below the central slice. The integral uniformity for each slice at all the displaced positions was calculated from equation [2].

$$IU_i = \frac{ROI_{max} - ROI_{min}}{ROI_{max} + ROI_{min}}$$ [2]

The integral axial uniformity was also calculated. To find the axial uniformity, the largest ROI mean value, $\overline{ROI_j}$ from slice j, and the smallest ROI mean value, $\overline{ROI_k}$ from slice k were determined. The integral axial uniformity was calculated from equation [3]:

$$IU_{axial} = \frac{\overline{ROI_j} - \overline{ROI_k}}{\overline{ROI_j} + \overline{ROI_k}}$$ [3]

The axial variability also served as an image quality metric. For each slice, seven circular ROIs with 60 mm diameter were drawn. One at the center of the phantom image, and the others arranged in a circle around it were drawn. The ROI mean, minimum, and maximum activity concentration for each ROI were recorded. The average and standard deviation of the seven ROI means for each slice were calculated. The averages, standard deviations, and standard deviation

/ average vs. slice number were plotted. SUVs were calculated by dividing the ROI mean, minimum, and maximum values by the known phantom activity concentration. The SUVs vs. slice number were plotted. ROI standard deviations, and standard deviations/average vs. ROI slice number were also plotted.

Line profiles were also used. The line profile was plotted across the middle of the circular cross-section and another line profile was plotted perpendicular to it for all the slices. The recorded activity concentrations were averaged over all slices. The threshold where the activity level may indicate the presence of relatively homogenous radioactive materials was identified and anything below it was zeroed out. The residuals of all the line profiles from the displaced phantoms in reference to the centered phantom were taken and the pattern of line profile change was examined. The minimum and maximum of the residual range were calculated. The standard deviations were also calculated for the line profiles.

2. METAL ARTIFACT STUDY

A. Data Acquisition

Two sets of experiments were performed to assess the effectiveness of the in-built metal artifact correction reconstruction algorithm (termed as whole-body metal contrast reconstruction) in resolving metal artifact in the CT image in comparison to the standard whole-body reconstruction. In the first experiment, ten steel alloy metal screws were attached on the top and side of the germanium-68 cylindrical phantom by adhesive tape. The activity concentration of the Ge-68 phantom was recorded. The phantom was subsequently placed at the center of

the PET/CT bore. Data were acquired by performing a whole-body PET/CT scan with standard whole-body reconstructions, where the surview image, CT image, non-attenuated-corrected PET image (NAC-PET) and attenuation-corrected PET image (CTAC-PET) were acquired. The frontal CT surview was used with the default parameters and three beds covering the entire Ge-68 phantom in the PET scan were performed with the acquisition time of 2 min per bed. The metal screws were subsequently detached keeping the phantom at the original position. Scanning was repeated with the same procedure and scan parameters in the absence of the metal screws and the images were exported. The images were reconstructed retrospectively with the specialized whole-body metal contrast reconstruction algorithm using the raw image stored on the server. This set of images was termed as 'the metal reconstruction with the presence of metals'. To further investigate the effectiveness or ineffectiveness of the metal reconstruction algorithm, the segmentation CT attenuation map generated after the CT acquisition was obtained.

In the second set of experiments, the quantity of the metal presence was increased to test the threshold for the effectiveness of the metal reconstruction. The phantom was kept at the center of the FOV with the attachment of three sets of double-layered metal plates (each with a thickness of approximately 3cm) on the top and on the two sides. The scanning procedure was performed in the same way as the first experiment, where the images with and without metal with the standard body reconstruction and the images reconstructed retrospectively with whole-body metal reconstruction were acquired.

B. Image Quality Analysis

ImageJ image processing tool was employed as the primary image processing tool and *Matlab* scripts were used to supplement for analysis. For both experiments, image quality was assessed on both global and localized scales. The global analysis was achieved by drawing regions of interest (ROI) centered at the center of the circular phantom with an area covering at least 80% of the total radioactive area. The ROI was maintained in a constant position with a similar area in all the phantom analyses. The ROI area, the mean activity concentration, the minimum and maximum activity concentration, the standard deviation and slice number were calculated. The activity concentrations were plotted against the slice number for all phantom positions. Standard uptake values were plotted against the slice number. This was achieved using the 'readcentroid.m' (see Appendix B) matlab script developed by the system analysis group.

Line profiles were also used. The line profile was plotted across the middle of the circular cross-section and another line profile was plotted perpendicular to it for all the slices using Matlab codes (See Appendix A). The activity concentrations were averaged over all the slices. The threshold where the activity level may indicate the presence of relatively homogenous radioactive materials was identified and anything below it was zeroed out. The residuals of all the line profiles from the displaced phantoms in reference to the centered phantom were calculated and the pattern of line profile change was examined. The minimum

and maximum of the residual range were calculated. The standard deviations of the line profiles were also obtained.

On a local scale, the slices containing metal streaking artifacts in the CT images were selected. The corresponding CTAC-PET image slices were identified. The ROI encircling the metal streaking artifact was drawn in the phantom on the selected slices. The ROI analysis was repeated as in the global analysis. The segmentation CT attenuation map with the slices of metal streaking artifacts in the first set of experiments was also selected for global and regional analysis.

III. RESULTS

1. OFF-CENTER STUDY

The activity concentration of Ge-68 phantom was 3.007mCi (or 111.3MBq) on 01-Jan-2010. The pellet was located at 130.1 arbitrary units when the phantom was placed at the laser-located center. The pellet was displaced to 100 and 200 arbitrary units respectively in the uppermost and lowermost allowable range. The phantom was also laterally displaced 15cm to the left and right respectively.

Figure 3 contains snapshots of the central slices for all the five acquisitions. They revealed various artifacts when the appropriate window and level were selected. The images at the center position, to the left and right and at the uppermost phantom position all (*Figure 3*, a,d,e,f) suffer from ringing artifact (15). Displaced positions also appear with lower homogeneity. Specifically, the upper-left side and bottom-right of the phantoms appear brighter at the uppermost and

lowermost pellet positions respectively. The visual interpretations serve as one source of evidence for the non-uniformity for images off the center.

Single ROI analysis was used for activity concentration (Figure 4 and 5), its standard deviation (*Figure 7*) and SUV (*Figure 6*). The activity concentration and SUV were significantly more variable across different slices when the phantom was at off-center positions. When the phantom was displaced vertically, the activity concentration and SUV were underestimated at the edges of the phantom, and was the most pronounced at the uppermost phantom position. When displaced laterally, the phantom overestimated activity concentration at the central portion while the edge of the phantom had a small degree of underestimation. This shows that the global activity concentration and SUV estimation inaccuracies originated from the non-uniformity, particularly at the edge of the scanning. The standard deviation analysis gives consistent yet slightly different interpretations. The center position shows a relatively constant and low standard deviation; displacements are all elevated at the edge, but not proportionally increased with the extent of displacement. This is consistent with the increased non-uniformity at the edge of the scanning, but does not have consistency with the difference of non-uniformity with the different directions of displacements.

A seven-ROI approach is also applied for the analysis (*Figure 8 and 9*). Similar outcomes were found as for the single ROI analysis, where the activity concentrations and SUVs at the edge are significantly under-estimated, particularly for the uppermost phantom position. The lateral displacement had

overestimated activity and SUV at the central portion. The SUV estimation inaccuracies, particularly at the edge, also exist on a more regional scale. It is consistent with the one-ROI analysis at the global level. For the standard deviation analysis in the seven-ROI approach, the center position remains relatively constant, yet at an elevated level, indicating enhanced local inhomogeneity due to the ringing artifact. Displacements except for the lowermost position display a similar trend as in the single-ROI analysis; at a lower position, the standard deviation is significantly elevated, but maintains relatively constant throughout different slices.

The integral uniformity and integral axial uniformity are shown in *Figure 12*. The displacement to the uppermost position results in the worst integral uniformity. The uppermost pellet position with significantly elevated level has the worst axial uniformity.

Line profiles were produced in Matlab (devised Matlab codes are supplemented in Appendix A), by sorting the dicom images into a three-dimensional matrix array and plotting line profiles across the origin of the circle (*Figure 10 and 11*). Horizontal and vertical line profiles were significantly more variable when the phantom was off-center. The range of the residuals in the horizontal line profiles was the highest when the phantom was placed at the displacement to the left and that in the vertical line profiles was the lowermost pellet position, where the edges of the phantom had higher activity level.
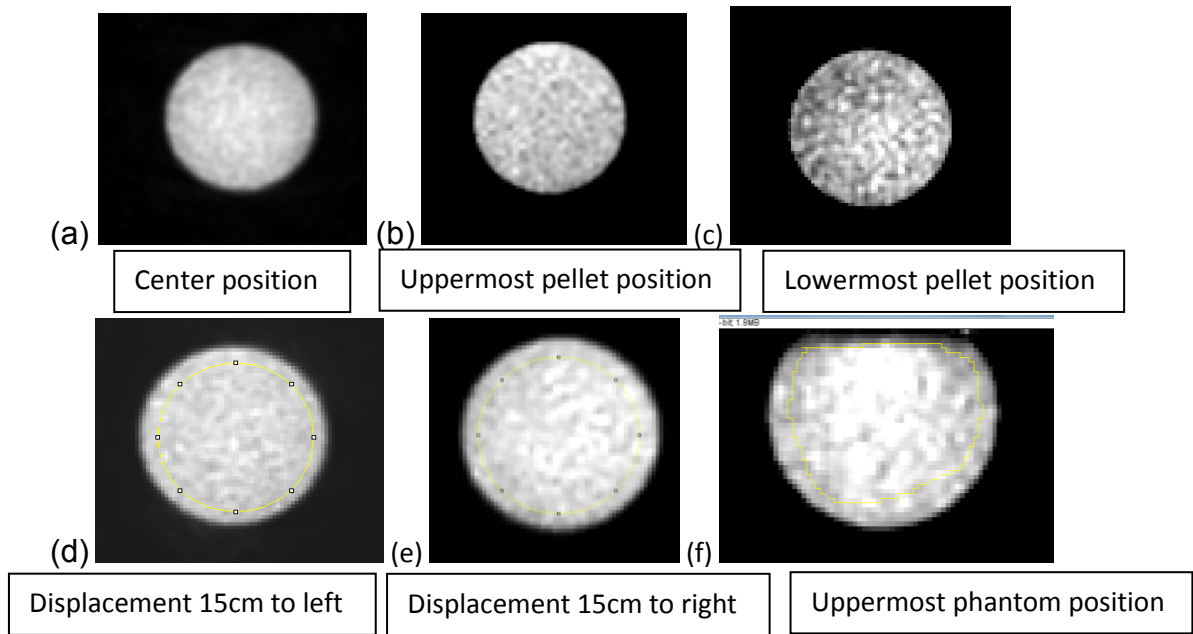
(a) Center position

(b) Uppermost pellet position

(c) Lowermost pellet position

(d) Displacement 15cm to left

(e) Displacement 15cm to right

(f) Uppermost phantom position

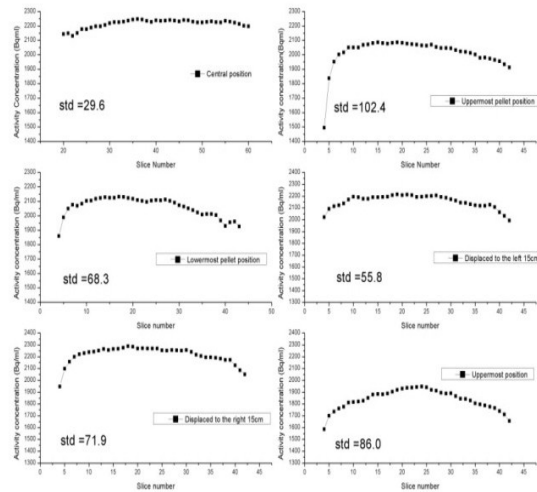**Figure 3:** The snapshots of the central slices at the six positions.

Figure 4: The activity concentration vs. slice number for the six phantom positions with the indication of the standard deviation of the activity concentration trend.
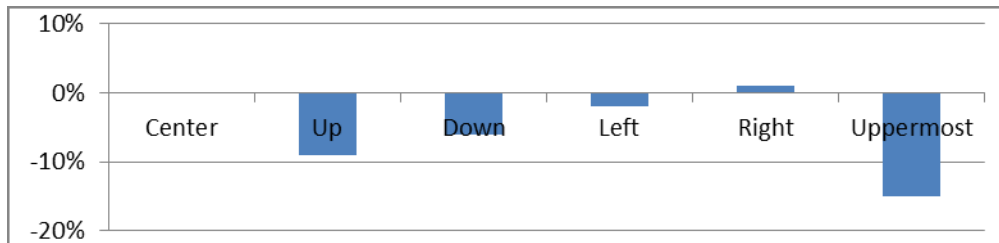
Figure 5: The percentage differences of the activity concentration at the central slice for the five positions relative to the center position.
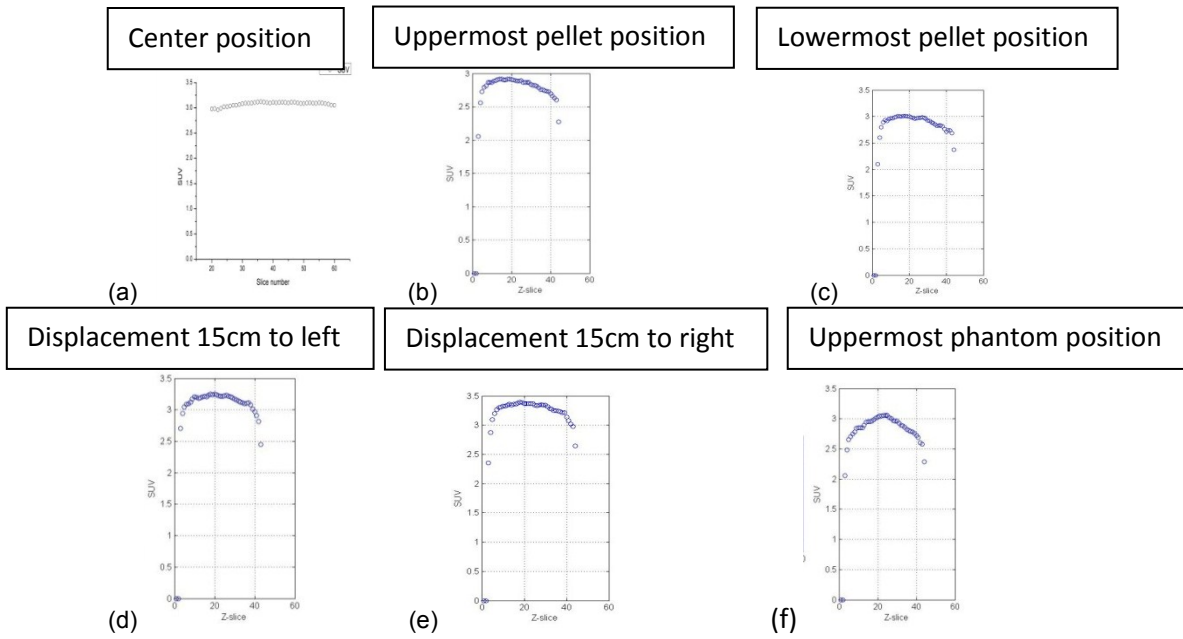
| Center position | Uppermost pellet position | Lowermost pellet position |

(a) (b) (c)

| Displacement 15cm to left | Displacement 15cm to right | Uppermost phantom position |

(d) (e) (f)

Figure 6: Standard Uptake Value (SUV) vs. slice number.
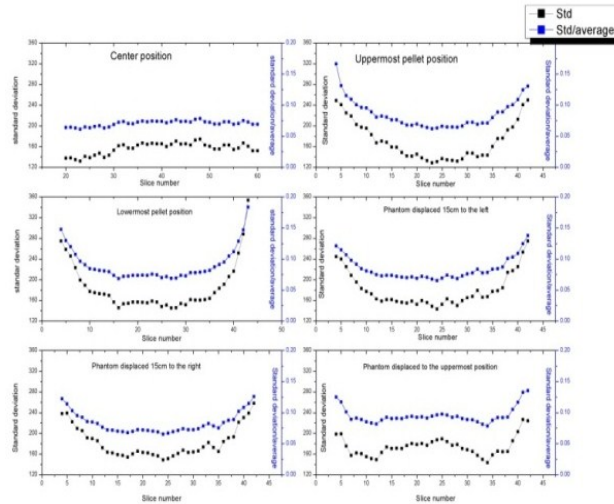

Figure 7: The standard deviation and the standard deviation/average activity concentration for the six phantom positions.
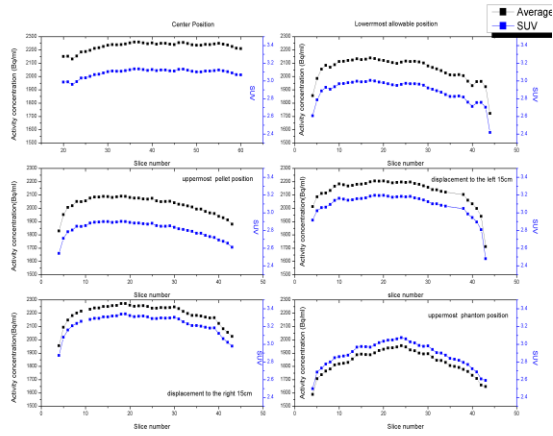
Figure 8: The activity concentration and the SUV in the seven-ROI approach for the six phantom positions.
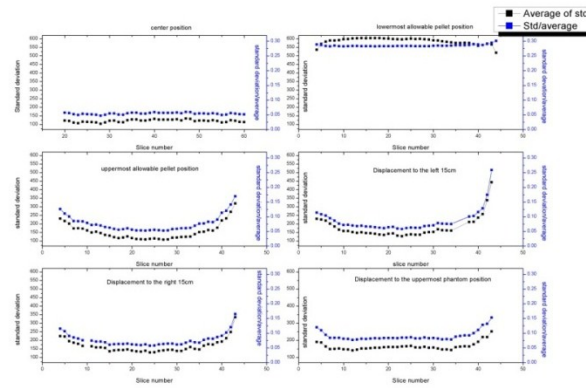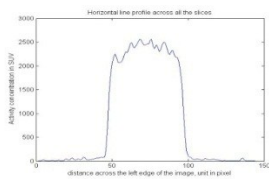

Figure 9: The standard deviation and the standard deviation/average in the seven-ROI approach for the six phantom positions.

Horizontal Line Profile

Center Position	Uppermost pellet position	Lowermost pellet position

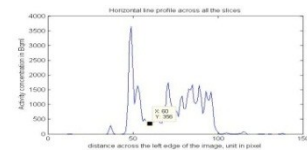| Displacement 15cm to the left	Displacement 15cm to the right	Uppermost phantom position
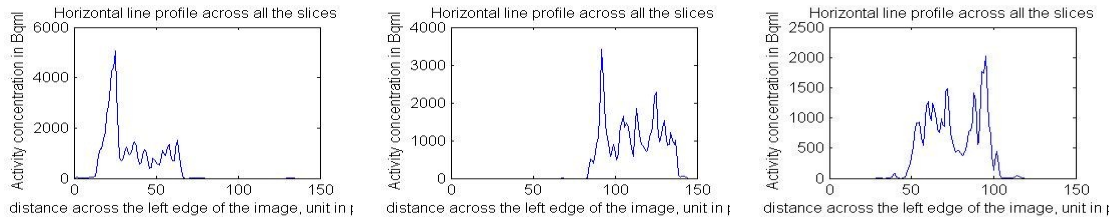
Vertical Line Profile

Center Position   Uppermost pellet position   Lowermost pellet position
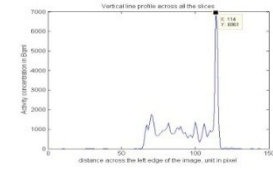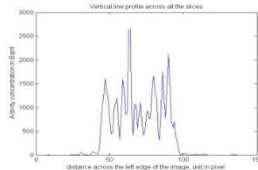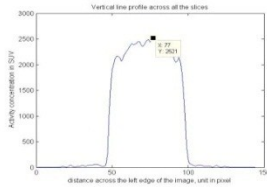
Displacement 15cm to the left   Displacement 15cm to the right   Uppermost phantom position
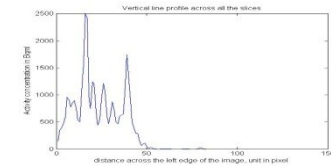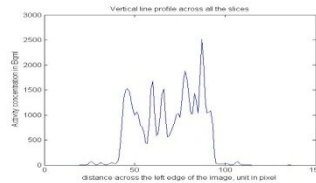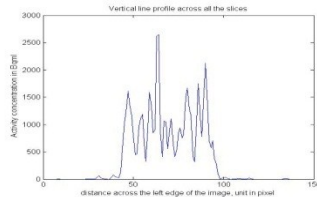
Figure 10: The horizontal and vertical line profiles of the six phantom positions.
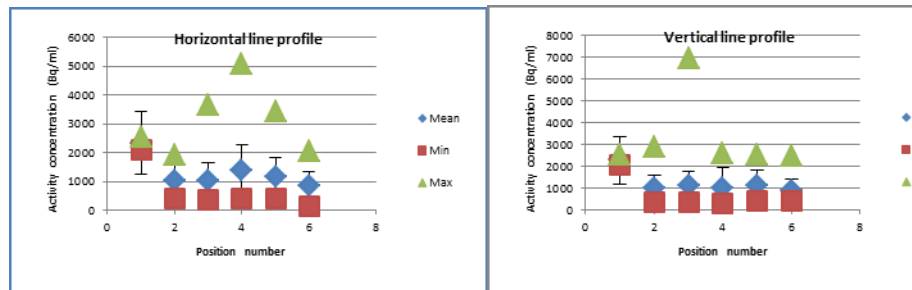
1) center position
2) uppermost allowable pellet position
3) lowermost allowable pellet position
4) displacement 15cm to the left
5) displacement 15cm to the right
6) phantom displacement to the uppermost position.

Figure 11: The minimum, maximum, mean and the standard deviation of the activity concentrations in

the horizontal and vertical line profile.

(b)

17
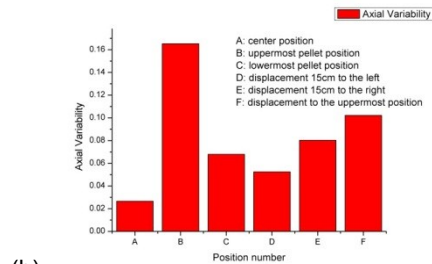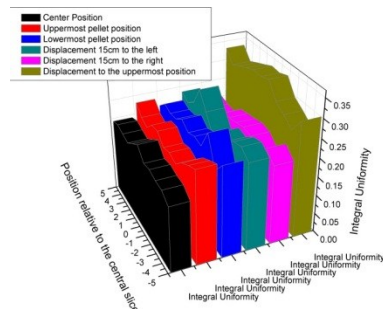
Figure 12: The integral uniformity and axial uniformity for the six phantom positions.

2. METAL ARTIFACT STUDY

The phantom activity was 103.6 MBq recorded on 1-Apr-2011. The global analysis for the first experiment with a small amount of metal present is shown in *Figure 13* and *Figure 14*, where the activity concentration, its standard deviation and the SUV are demonstrated. Line profiles with analysis are indicated in *Figure 15*. With the presence of a small amount of metal, the activity concentration is changed in comparison to that without the metal; however, the CTAC and whole-body metal contrast reconstruction have virtually no difference in the activity concentration and its standard deviation in the overall image quality, as well as the SUV values in the image. The line profiles also have negligible differences. At the region of the most severe metal artifact, slight differences between the activity concentration and its standard deviation exist, particularly for the slices at the central position. The analysis of the CT attenuation map shown in *Figure 16* helps to explain these differences: the differences in the activity concentration and standard deviation correspond to the differences in the attenuation coefficients at these localized regions.

The regional analysis for the first experiment for the regions of metal streaking artifacts is demonstrated in *Figure 17*, where the activity concentration and standard deviation at a localized ROI is compared. *Figure 18* shows the line profiles across the metal artifacts in the slices containing metals. *Figure 19* shows the segmentation attenuation map at the localized ROI of metal artifacts.

18

(a) (b)
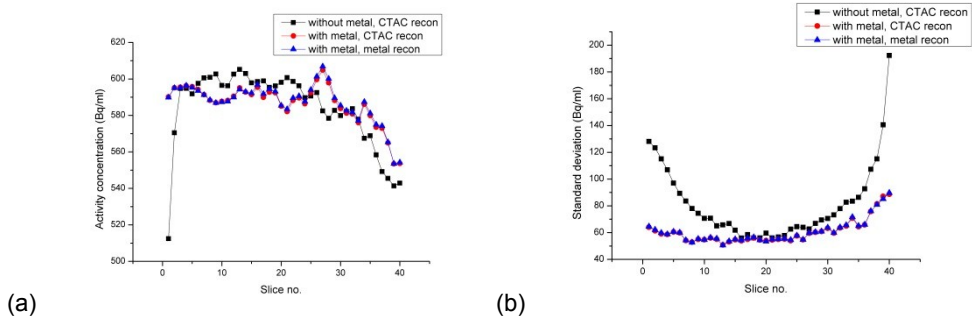
Figure 13: The activity concentration and its standard deviation with the two reconstruction methods.

(a) (b)
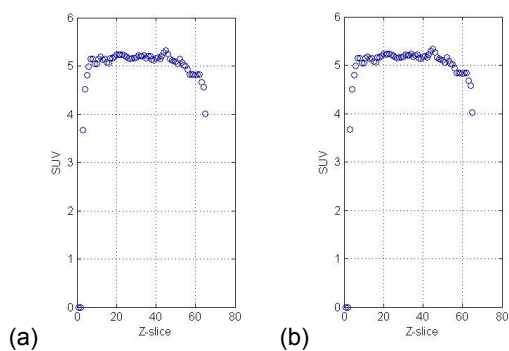
Figure 14: The standard uptake values (SUV) of the two reconstruction methods.

Standard deviation = 135.2353

Standard deviation = 107.0041

(a)

Standard deviation = 135.8255

Standard deviation = 107.5065

(b)
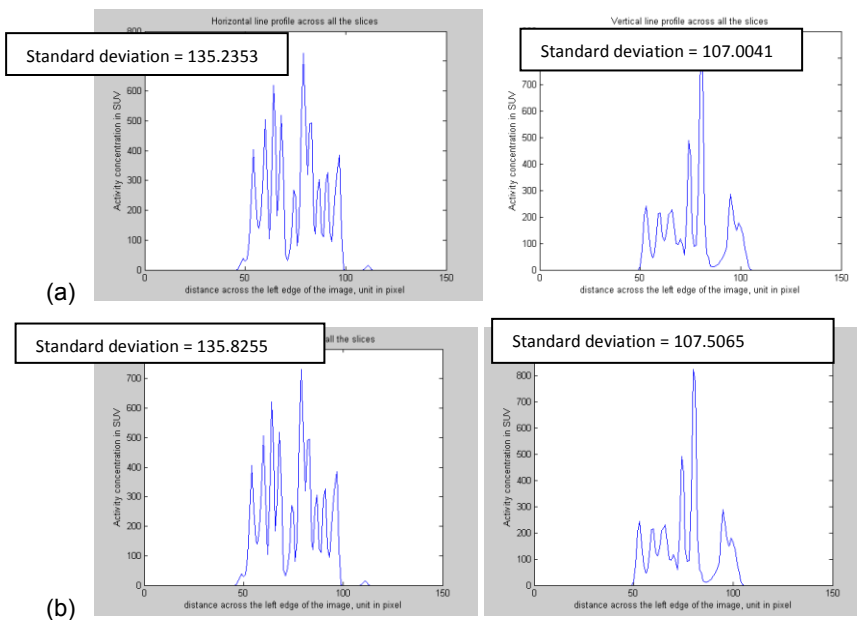
Figure 15: The horizontal and vertical line profiles for a) CTAC b) whole-body metal reconstructions.

19

(a)   (b)
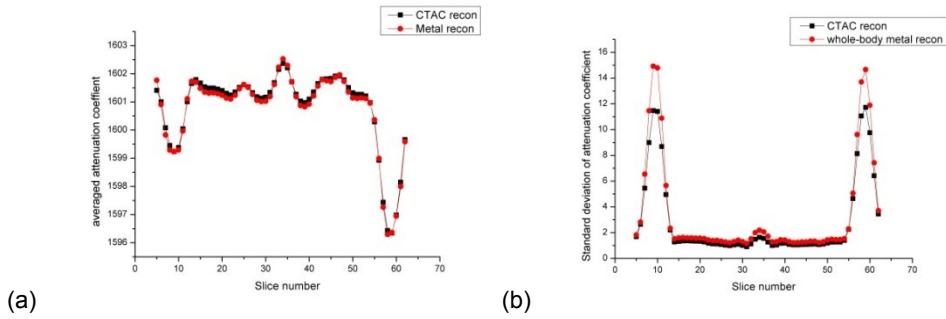
Figure 16: The averaged attenuation coefficient (a) and its standard deviation (b) for the two reconstruction methods.

(a)   (b)
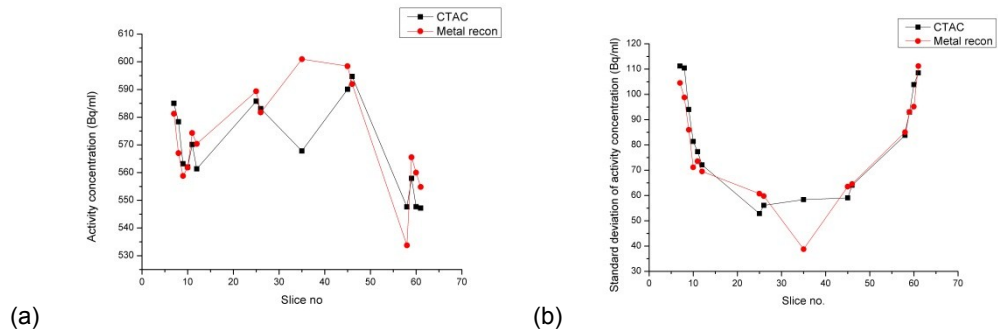
Figure 17: The averaged activity concentration (a) and its standard deviation (b) at localized regions containing metal artifacts with the two reconstruction methods.

(a)   (b)
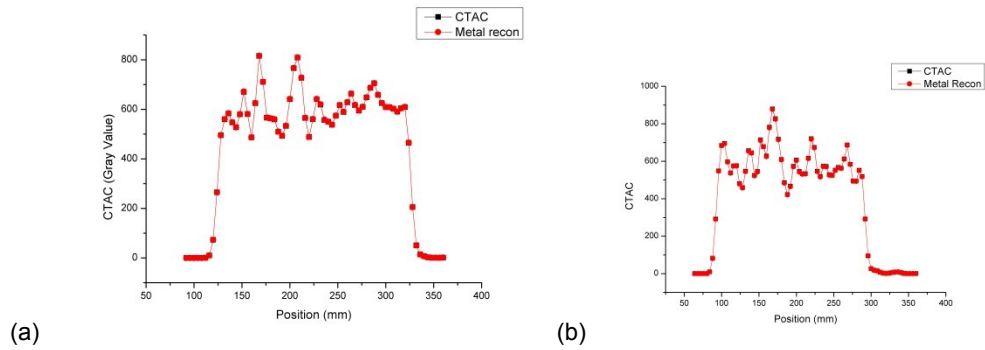
Figure 18: The line profile across the metal streaking artifact in slice 9 (a) and slice 59 (b).

(a)

(b)
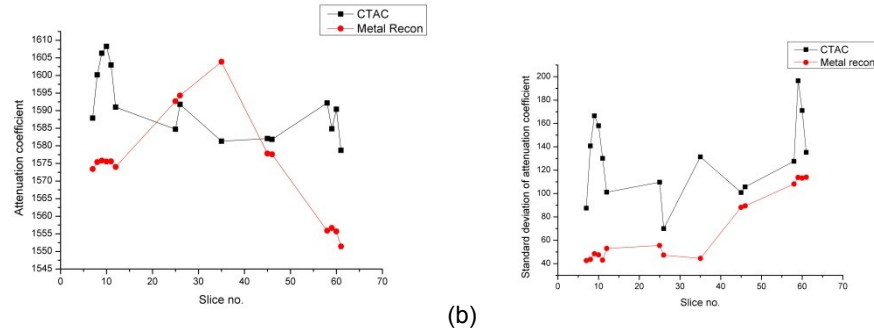
Figure 19: The averaged attenuation coefficient (a) and its standard deviation (b) of the segmentation CT map.

The global analysis for the second experiment where large quantity of metal is present is shown in *Figure 20*, where the activity concentration and its standard deviation of the two reconstruction methods are compared. The standard uptake values are compared in *Figure 21*. The line profiles are shown in *Figure 22*. The global analysis also shows similar activity concentration, standard deviation and line profiles for both reconstructions.

A representative CT image is shown in *Figure 23*, where regions of severe metal artifacts are selected for regional analysis. The regional activity concentration and its standard deviation are shown in *Figure 24*. At regions of the most severe metal artifact (the region of the top metal plate), the activity concentration and standard deviation have negligible differences.

21

(b)
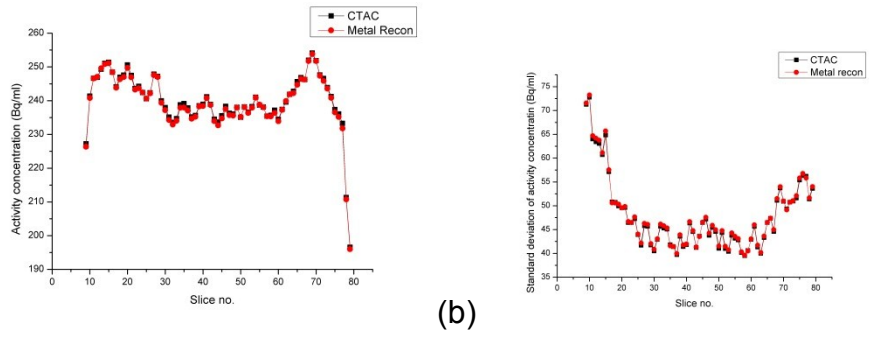
Figure 20: The activity concentration (a) and its standard deviation (b) with large metal presence.

(a)   (b)
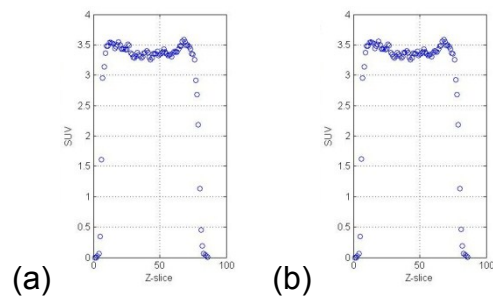
Figure 21: The SUVs of the CTAC (a) and metal (b) reconstructions.

Standard deviation = 0.1858

Standard deviation = 0.4969

(a)

Standard deviation = 0.1858

Standard deviation = 0.4969

(b)
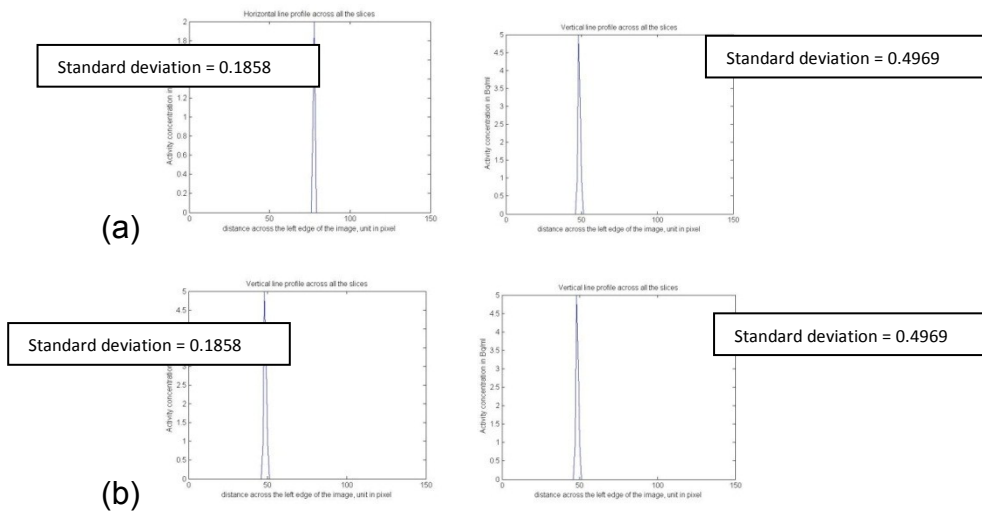
Figure 22: The line profiles of a) CTAC and b) metal reconstructions.
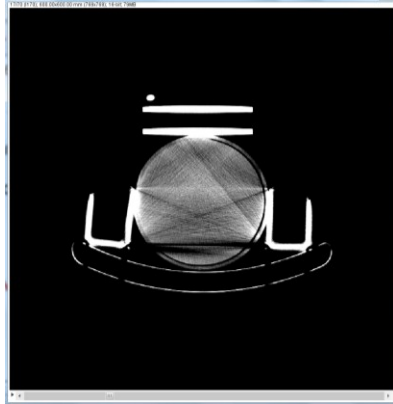
Figure 23: A representative CT image.

(a)   (b)
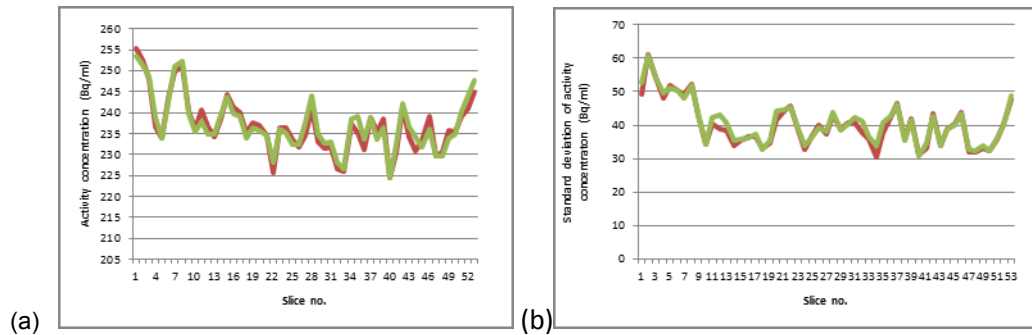
Figure 24: The regional analysis of a) averaged activity concentration and b) its standard deviation.

IV. DISCUSSION

1. OFF-CENTER STUDY

The non-uniformity for the off-center displacements is demonstrated in multiple analyses. The visual interpretations for the snapshots of the scanning qualitatively demonstrate the non-uniformity at the displaced positions. The homogeneity of image quality across different slices can be quantitatively assessed in four ways. The standard deviation and the standard deviation/average of a large ROI reflect the global change of activity concentration. When the ROIs are segmented into seven smaller ones, regional fluctuations are better represented. Integral uniformity and axial uniformity, which

23

rely on the maximal and minimal values, best reflect the regional spikes in the image quality. Line profiles represent the change of activity concentration across the phantom averaged over all the slices: a perfectly homogenous phantom has the line profile of a rectangular function. These four methods provide a comprehensive way to assess image quality. Additionally, non-uniformity generally leads to signal inaccuracies, which can be demonstrated both for activity concentration and SUV at both a global and a regional level by activity concentration and SUV trend across all the slices. The quantitative analysis is consistent with the qualitative interpretations, where non-uniformity for the displaced positions is signified. Non-uniformity generally leads to signal inaccuracies, which are demonstrated both for activity concentration and SUV at both a global and a regional level. The signal accuracy is generally degraded at the two ends of the object when the phantom is off the center. Vertical displacement suffers from the overall underestimation of signal intensities whereas lateral displacement overestimates the central portion. The standard deviation analysis shows significantly elevated standard deviation at the edge of the scanning; yet the non-uniformity deduced from standard deviation does not seem to depend on either the direction or the degree of displacement.

It is generally established in the imaging industry that the acceptance criteria for PET/CT performance is to have activity concentration at displaced positions within 10% difference in comparison to the center position. The analysis shows that the displacement within the allowable pellet position and within 15cm in the lateral direction has acceptable imaging performance, particularly in the lateral

direction, where the difference could originate from measurement variation, rather than the actual performance differences. The displacement to the uppermost position, nevertheless, has a significant under-estimation of the activity concentration beyond the acceptance limit. It becomes worse towards the edge, where the activity concentration drops by up to 30% and significantly degrades the accuracy of measurement.

The horizontal and vertical line profiles are consistent with the standard deviation study, where the non-uniformity also does not appear to depend on the direction or the extent of the displacement, but it is significantly increased off the center.

Integral uniformity serves to demonstrate the range of the residuals across the central slices: the smaller the value, the better the uniformity of the image. The displacement to the uppermost position results in the worst integral uniformity. Axial uniformity shows the variation across the phantom and the uppermost pellet position has a significantly elevated level. This demonstrates that the vertical displacement in the upper direction appears to generate the largest global fluctuations in the activity concentration estimation.

These results indicate that displacement off the center affects the signal accuracy and the uniformity of the image. Position off the center has three major impacts on image quality: 1) objects at the two ends are more prone to non-uniformity 2) displacement in the vertical direction has larger signal deviation than that in the lateral direction 3) displacement at the extreme degree to the far edge of the bore results in the largest signal measurement inaccuracy, but not

necessarily the largest non-uniformity. These performance flaws with displacement of radioactive source shed light to the potential imperfections of the scanner properties, design and reconstruction algorithms. The off-center problems could be from a number of different possibilities; one of which is the change in photon scatter when the source is displaced and the failure to correct for it with the currently used reconstruction algorithm. Further investigation of the scatter correction in the reconstruction with specially designed phantoms (16, 17) will aid in determining for the cause of the increased non-uniformity. It is important to note that the conclusion from the uppermost phantom position may not be relevant to the extreme lateral displacement, which is a lot more common in the clinical setting and this should be experimentally evaluated in the future.

2. METAL ARTIFACT STUDY

The presence of a small amount of metal generated virtually no difference in the global activity concentration, SUV and standard deviation as well as line profiles. This can be explained by the virtually identical global attenuation coefficients for the two reconstructions. The regional differences, although very small, can be explained by the attenuation coefficient differences. The metal reconstruction algorithm generally has reduced attenuation coefficients. The high proton absorption by metal increases the Hounsfield units, which correspondingly leads to increased PET attenuation coefficients. This is mostly effectively corrected by the whole-body metal contrast reconstruction, which shows reduced attenuation coefficients in comparison to CTAC. However, the large attenuation coefficient differences for the slices at the edge generate similar activity concentrations.

One possible explanation is that the differences in attenuation coefficients are too small to lead to significant change in activity concentration, possibly due to the small amount of metal present. When the amount of metal is increased as in the case of the second experiment, the global analysis also shows similar activity concentration, standard deviation and line profiles for both reconstructions. At regions of the most severe metal artifact (the region of the top metal plate), the activity concentration and standard deviation have negligible differences. As the attenuation map is not acquired in the second experiment, the attenuation change with the metal contrast reconstruction is uncertain; nevertheless, the attenuation coefficient does not significantly impact the activity concentration. This shows that the in-built metal reconstruction method does not significantly improve image quality that is degraded by metal streaking artifact, both for the presence of the small amounts of metal (on the scale of mm) or larger amount of metal (on the scale of cm). The overall image quality at a global level is virtually unperturbed; at a local level, the small amount of decreased attenuation coefficient with the whole-body metal contrast reconstruction does not result in a significant change in the image quality, for both small and large amount of metal present. The inefficacy of the whole-body metal contrast reconstruction may originate from the reconstruction algorithm, where metal and bone are assumed to have the same Hounsfield unit. The differences between the two, however, cannot be neglected: at 100 keV of photon energy, the linear attenuation coefficient of iron is 2.93/cm (18), while that of cortical bone is 0.356/cm (19). As the linear attenuation coefficient of soft tissue is around 0.160/cm (19), this

algorithm significantly underestimates the iron attenuation ability and poorly differentiates between metal artifacts and the background soft tissues. It leads to under-compensation for metal artifact and the inefficacy of the reconstruction for metal with thickness up to 3cm. The consequences of the study are two-fold: first, the image quality from the standard CTAC is sufficient with metal artifact and the option with the whole-body metal contrast reconstruction becomes redundant; second, neither CTAC nor metal contrast reconstruction provides sufficient image quality for metal artifacts. A better reconstruction algorithm is needed to address this problem.

This conclusion cannot be directly applied to the clinical setting. Firstly, the composition and the weight of the metal presence used in the experiments does not match that of metallic implants; further analysis with better quantification of the metal composition will improve the generalization of the outcome. Secondly, all the metal in the experiments are attached on the outer layer of the phantom. In clinical cases, metallic implants are positioned within a patient's body and it will be preferable to replace the cylindrical phantom with a whole-body anthropomorphic phantom or a scatter phantom (20), where the metal can be inserted or placed at the positions for appropriate clinical situations, particularly to be surrounded by materials with attenuation coefficients resembling that of soft tissues. Thirdly, the threshold of the metal could be further increased by attaching thicker metal plates onto the phantom.

V. CONCLUSION

In this study, two PET performance tests – the off-center study and the metal artifact study – were conducted for the evaluation of a new PET/CT scanner. Displacement off the center results in increased non-uniformity, particularly at the edge, and the activity concentration and SUV inaccuracies worsen with increased degree of displacement. The in-built whole-body metal contrast reconstruction fails to correct for the metal artifact. The results are critical for the development of new PET/CT system with improved image quality. Further work is required for both studies to better represent clinical conditions and for a more detailed investigation on the cause of such system failures.

VI. REFERENCE

(1) Saha, G. B. (2010). Performance Characteristics of PET Scanners. <u>Basics of PET Imaging: Physics, Chemistry, and Regulations</u>, Springer Science.

(2) Boellaard, R. (2009). "Standards for PET image acquisition and quantitative data analysis." <u>J Nucl Med</u> **50 Suppl 1**: 11S-20S.

(3) *Performance Measurements of Positron Emission Tomographs.* Rosslyn, VA: National Electrical Manufacturers Association; 2007. NEMA Standards Publication NU 2-2007.

(4) Watson, C. C., M. E. Casey, et al. (2004). "NEMA NU 2 performance tests for scanners with intrinsic radioactivity." <u>J Nucl Med</u> **45**(5): 822-826.

(5) Gemini TF PET/CT, Philips Healthcare, <u>http://www.healthcare.philips.com/us_en/products/nuclearmedicine/products/geminitf/</u> (update on 31-Aug-2012).

(6) Buchert, R., K. H. Bohuslavizki, et al. (2000). "Performance evaluation of PET scanners: testing of geometric arc correction by off-centre uniformity measurement." <u>Eur J Nucl Med</u> **27**(1): 83-90.

(7) Goerres, G. W., T. F. Hany, et al. (2002). "Head and neck imaging with PET and PET/CT: artefacts from dental metallic implants." <u>Eur J Nucl Med Mol Imaging</u> **29**(3): 367-370.

(8) Kamel, E. M., C. Burger, et al. (2003). "Impact of metallic dental implants on CT-based attenuation correction in a combined PET/CT scanner." <u>Eur Radiol</u> **13**(4): 724-728.

(9) Sureshbabu, W. and O. Mawlawi (2005). "PET/CT imaging artifacts." <u>J Nucl Med Technol</u> **33**(3): 156-161; quiz 163-154.

(10)   (2006). PET: Physics, Instrumentation, and Scanners. <u>Michael E. Phelps</u>, Sringer**:** 106.

(11)   Bailey, D.J. and Jones T. (1996). "An Investigation of Factors Affecting Detector and Geometric Correction in Normalization of 3-D PET Data." <u>IEEE Transactions on Nuclear Science</u> **43** (6), 3300-3307.

(12)   Brown, C., M. F. Dempsey, et al. (2010). "Investigation of 18F-FDG 3D mode PET image quality versus acquisition time." <u>Nucl Med Commun</u> **31**(3): 254-259.

(13)   Miller M.A and Jordan D.W (2012). "PET image uniformity assessment." Draft, Philips Internal Use.

(14)   Dwivedi, A., A. Malhotra, et al. (2011). <u>Radiation exposure to nuclear medicine personnel handling positron emitters from Ge-68/Ga-68 generator</u>.

(15)   Ay, M.A., Sarkar S. (2007), "Computed Tomography Based Attenuation Correction in PET/CT: Principles, Instrumentation, Protocols, Aritifacts and Future Trends.", <u>Iron J Nucl Med</u> **15**(2), 1-29.

(16)   El-Ali, H., M. Ljungberg, et al. (2003). "Calibration of a radioactive ink-based stack phantom and its applications in nuclear medicine." <u>Cancer Biother Radiopharm</u> **18**(2): 201-207.

(17)   Van Laere, K. J., J. Versijpt, et al. (2002). "Experimental performance assessment of SPM for SPECT neuroactivation studies using a subresolution sandwich phantom design." <u>Neuroimage</u> **16**(1): 200-216.

(18)   Linear attenuation coefficient of selected elements, <u>http://www.astm.org/BOOKSTORE/DS68/pg53.pdf</u> (update on 31-Aug-2012)

(19)   Webb, S. X-ray transmission computed tomography. <u>The Physics of Medical Imaging</u>. Bristol and Philadelphia, Adam Hilger**:** 99.

(20)   Ay, M. R., A. Mehranian, et al. (2011). "Qualitative and quantitative assessment of metal artifacts arising from implantable cardiac pacing devices in oncological PET/CT studies: a phantom study." <u>Mol Imaging Biol</u> **13**(6): 1077-1087.

V. APPENDIX
APPENDIX A

The codes are used for generating the line profile at the displacement to the left

as an experiment.

```matlab
%% Load the image and save them as 4D matrix array

temp_img = dicomread('I10');
header_img = dicominfo('I10');
matrix = zeros (header_img.Height, header_img.Width,
header_img.NumberOfSlices);
%[file path] = uigetfile('*.*','Load DICOM files');
path = 'C:\Philips\REPORTS\metal_artifact\metal_recon\S3600\S14790\';
files = dir(strcat(path,'I*'));
fnums = zeros(length(files),1); %How many files start with I*
for i = 1:length(files)
    fnums(i)=str2double(files(i).name(2:end)); %name(2:end) because
files.name is I10,I20
    ...so you get the numbers of the file to sort it numerically
end
[b,ix]=sort(fnums);
files=files(ix);
%save them as 4D matrix array
for k =1: header_img.NumberOfSlices
    matrix(:,:,k)= dicomread(files(i).name);
end
figure
imshow(matrix (:,:,20),[]);
%% Calculate line profiles --average over all the slices
% Horizontal line profile
cross_hon = matrix(header_img.Height./2,:,:);
for i= 1: header_img.Width
cross_mean_hon(1,i) = mean (cross_hon(:,i,:));
end
%plot the line profile
figure (1)
plot (cross_mean_hon)
xlabel('distance across the left edge of the image, unit in pixel')
ylabel('Activity concentration in Bq/ml')
Title ('Horizontal line profile across all the slices')
%Calculate the standard deviation of numbers above the threshold of
0.01
threshold = 0.01;
for i = 1:1: header_img.Width
if cross_mean_hon(1,i)<threshold
    cross_mean_hon(1,i)=0;
else
    cross_mean_hon(1,i)= cross_mean_hon(1,i);
end
```

```matlab
end
cross_sdv_hon = std(cross_mean_hon)
% Calculate vertical line profile
cross_ver = matrix(:,header_img.Width./2,:);
for i= 1: header_img.Height
cross_mean_ver(i,1) = mean (cross_ver(i,:,:));
end
%plot the line profile
figure (2)
plot (cross_mean_ver)
xlabel('distance across the left edge of the image, unit in pixel')
ylabel('Activity concentration in Bq/ml')
Title ('Vertical line profile across all the slices')
%Calculate the standard deviation of numbers above the threshold of
0.01
threshold = 0.01;
for i = 1:1: header_img.Height
if cross_mean_ver(i,1)<threshold
    cross_mean_ver(i,1)=0;
else
    cross_mean_ver(i,1)= cross_mean_ver(i,1);
end
end
cross_sdv_ver = std(cross_mean_ver)
```

APPENDIX B

The readcentroid.m matlab code developed by the system analysis group at

Philips Healthcare is shown as the followings:

```
clear all;
plot_flag = 0;
% [file path] = uigetfile('*.*','Load DICOM files');
% path
%
='C:\Users\usd22786\Desktop\SE1.3.46.670589.28.2.12.21.6136.17012.2.165
6.0.1344522778\'; %WIP602.1 SUV Val 256
path
='C:\Philips\REPORTS\metal_artifact\metal_recon\S3600\S14790\'; %WIP602
.1 SUV Val 576
% path = 'C:\Users\usd22786\Desktop\OSU Mobile\DICOM
images\ACRIN\S103490\S909800\';%ACRIN Brain
% path = 'C:\Users\usd22786\Desktop\OSU Mobile\DICOM
images\ACRIN\S103480\S893100\';%ACRIN Body
% path = 'C:\Users\usd22786\Desktop\OSU Mobile\DICOM images\SUV
Val\S103470\S769200\';%SUV Val Brain
% path = 'C:\Users\usd22786\Desktop\OSU Mobile\DICOM images\SUV
Val\S103460\S631100\';%SUV Val TF Body
% path = 'C:\Users\usd22786\Desktop\OSU Mobile\DICOM images\SUV
Val\S103460\S651300\';%SUV Val R3D Body
% path = 'C:\Users\usd22786\Desktop\Solo\data\MCSSS re-
recons\Brain\S940\S11360\'; %TF Brain MC SSS
% path = 'C:\Users\usd22786\Desktop\Solo\data\MCSSS re-
recons\Brain\S940\S21150\'; %TF Brain Ivan SSS
% path = 'C:\Users\usd22786\Desktop\Solo\data\MCSSS re-
recons\Brain\S920\S11270\'; %576 SUV MC SSS
% path = 'C:\Users\usd22786\Desktop\Solo\data\MCSSS re-
recons\Brain\S920\S21110\'; %576 SUV Ivan SSS
% path = 'C:\Users\usd22786\Desktop\Solo\data\2012-07-12-Solo-Bay11-
SUV-ACRIN\DICOM images\ACRIN Brain\S13470\';
% path = 'C:\Users\usd22786\Desktop\Solo\data\2012-07-12-Solo-Bay11-
SUV-ACRIN\DICOM images\ACRIN Body\S13400\';
% path = 'C:\Users\usd22786\Desktop\Solo\data\2012-07-12-Solo-Bay11-
SUV-ACRIN\DICOM images\SUV 256\S13650\';
% path = 'C:\Users\usd22786\Desktop\Solo\data\2012-07-12-Solo-Bay11-
SUV-ACRIN\DICOM images\SUV 576\S13510\';
% path = 'C:\Users\usd22786\Desktop\Solo\data\2012-07-12-Solo-Bay11-
SUV-ACRIN\DICOM images\SUV 576 higher\S13340\';

%Sort DICOM files if names are I*
files = dir(strcat(path,'I*'));
fnums = zeros(length(files),1); %How many files start with I*
for i = 1:length(files)
    fnums(i)=str2double(files(i).name(2:end)); %name(2:end) because
files.name is I10,I20
```

```matlab
        ...so you get the numbers of the file to sort it numerically
end
[b,ix]=sort(fnums);
files=files(ix);

% %If files are .dcm
% files = dir(strcat(path));
% for i = 3:length(files)-1
%     fnums(i-2)=hex2dec((strtok(files(i).name,'.')));
% end
% [b,ix]=sort(fnums);
% files=files(ix);

fname = strcat(path,files(3).name);
headers{1} = dicominfo(fname);
rows = double(headers{1,1}.Rows);
cols = (rows);
resolution = headers{1,1}.PixelSpacing(1);

%Calculate Centroid [mx,my]
x = ones(rows,1)* (1:cols);
y = (1:rows)'*ones(1,cols);
fname = strcat(path,files(ceil(length(files)/2)).name);
img_temp = int16(dicomread(fname));
% im = img_temp>400; %threshold level
im = img_temp>100; %threshold level for TF brain
area = sum(sum(im));
mx = floor(sum(sum(double(im).*x))/area);
my = floor(sum(sum(double(im).*y))/area);


h = waitbar(0,'Loading files');%Load the files
% for i=1:length(files)
 for i=3:length(files) -1
    fname = strcat(path,files(i).name);
    img(:,:,i) = int16(dicomread(fname));
    headers{i} = dicominfo(fname);
    waitbar(i/length(files),h);
 end
close(h);

R = ceil(75/resolution);
[rr cc] = meshgrid(1:rows);
C = sqrt((rr-mx).^2+(cc-my).^2)<=R;
% imagesc(C); axis square;

% % For overlay, Draw ROI with center at [mx,my] and radius R

N=50;
theta = linspace(0,2*pi,N);
[X,Y] = pol2cart(theta,R);
X = X + mx;
Y = Y + my;


%
```

```matlab
% for i=1:length(files)
for i=3:length(files) -1
    im = img(:,:,i);
    mean_roi(i) = mean(mean(im(C)));
if strcmp(headers{i}.Units,'BQML')
    plot_flag=1;
    mean_roi_bqml(i) = mean_roi(i)*headers{i}.Private_7053_1009;
    mean_roi_suv(i) = mean_roi(i)*headers{i}.Private_7053_1000;
end
end
% figure;

%Activity in the phantom
half_life =
headers{1}.RadiopharmaceuticalInformationSequence.Item_1.RadionuclideHa
lfLife;

a = (headers{1}.AcquisitionTime);
acq_time = str2double(a(1:2))*3600 + str2double(a(3:4))*60 +
str2double(a(5:6));
a =
headers{1}.RadiopharmaceuticalInformationSequence.Item_1.Radiopharmaceu
ticalStartTime;
inj_time = str2double(a(1:2))*3600 + str2double(a(3:4))*60 +
str2double(a(5:6));
decay_time = acq_time - inj_time;

A0 =
(headers{1}.RadiopharmaceuticalInformationSequence.Item_1.RadionuclideT
otalDose);
act = A0*power(2,-decay_time/half_life);
act_conc = act/(headers{1}.PatientWeight*1000);
suv = 1;

% mc576 = mean_roi_suv;
% ivan576 = mean_roi_suv;




% Plots
% figure;
% subplot 221; imagesc(img(:,:,20)); axis square; hold on;
plot(X,Y,'k*');
% h = title({headers{1}.SeriesDescription});
% set(h,'interpreter','none');
%
% subplot 222, plot(mean_roi/max(mean_roi)*100,'b.'); xlabel('Z-slice');
ylabel('Counts');grid on; %normalized to max
% h = title({headers{1}.PatientID});
% set(h,'interpreter','none');
%
% while plot_flag
% subplot 223, plot(mean_roi_bqml,'bo'); xlabel('Z-slice');
ylabel('Bq/mL');
```

```matlab
% hold on; plot(1:length(files),act_conc,'k-
');plot(1:length(files),act_conc*1.05,'r*');plot(1:length(files),act_co
nc*.95,'r*');hold off;
% h = title({headers{1}.ProtocolName});
% set(h,'interpreter','none');
%
% subplot 224, plot(mean_roi_suv,'bo'); xlabel('Z-slice');
ylabel('SUV'); grid on;
% hold on; plot(1:length(files),suv,'k-
');plot(1:length(files),suv*1.05,'r*');plot(1:length(files),suv*.95,'r*
');hold off;

% for i = 1:10
%     skip = i-1;
%     var_suv(i) = (max(mean_roi_suv(1+skip:end-skip))-
min(mean_roi_suv(1+skip:end-skip)))/mean(mean_roi_suv(1+skip:end-
skip))*100;
% end
% subplot 222, plot(3:length(var_suv),var_suv(3:end),'o'); grid on;
xlabel('Edge Slices skipped');ylabel('%Variability');
% break;
% end

figure;
subplot 121; imagesc(img(:,:,20)); axis square; hold on; plot(X,Y,'k*');
h =
title({headers{1}.SeriesDescription,headers{1}.PatientID,headers{1}.Pro
tocolName,headers{1}.AcquisitionDate});set(h,'interpreter','none');

subplot 122, plot(mean_roi_suv,'bo'); xlabel('Z-slice'); ylabel('SUV');
grid on;
% hold on; plot(1:length(files),suv,'k-
');plot(1:length(files),suv*1.05,'r*');plot(1:length(files),suv*.95,'r*
');hold off;

% subplot 122, plot(mean_roi/max(mean_roi)*100,'bo'); xlabel('Z-slice');
ylabel('Counts');grid on; %normalized to max
```
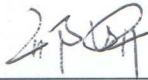
Publishing Agreement

It is the policy of the University to encourage the distribution of all theses, dissertations, and manuscripts. Copies of all UCSF theses, dissertations, and manuscripts will be routed to the library via the Graduate Division. The library will make all theses, dissertations, and manuscripts accessible to the public and will preserve these to the best of their abilities, in perpetuity.

Please sign the following statement:

I hereby grant permission to the Graduate Division of the University of California, San Francisco to release copies of my thesis, dissertation, or manuscript to the Campus Library to provide access and preservation, in whole or in part, in perpetuity.

_____   SEP - 11 - 2012
Author Signature   Date